MITSUBISHI ELECTRIC RESEARCH LABORATORIES
https://www.merl.com

Simultaneous Range and Velocity Measurement with Doppler Single-Photon Lidar

Kitichotkul, Ruangrawee; Rapp, Joshua; Ma, Yanting; Mansour, Hassan

TR2025-050 April 26, 2025

Abstract

Single-photon lidar (SPL) can accurately measure distances to targets from extremely weak reflections. However, the conventional wisdom holds that pulsed lidar cannot directly measure velocity, unlike other forms of lidar. We present for the first time a detection model for SPL that explicitly includes a target's radial velocity, manifesting as a Doppler shift in the repetition frequency of the received laser pulse train. We propose an approach called Doppler SPL, comprising a pair of methods for jointly estimating range and velocity. Our first method estimates the Doppler shift via Fourier analysis of the detection times. The second method is a maximum likelihood (ML) estimator that can improve the Fourier estimate, and which also enables joint estimation of the flux from signal and background sources. We derive the Cramér–Rao bound for the estimation problem and show via simulations that the ML estimator is statistically efficient across diverse acquisition settings. We also demonstrate simultaneous estimation of range with sub-centimeter accuracy and velocity with 0.1 m/s root mean square error for experimental measurements at 50 frames per second, despite a signal-to-background ratio as low as 0.007. Finally, we present an example of a 3D video reconstruction at 120 fps with per-pixel velocity estimates. With the addition of velocimetry, Doppler SPL has the potential to introduce new capabilities in applications such as atmospheric monitoring or autonomous navigation.

Optica 2025

Mitsubishi Electric Research Laboratories, Inc.
201 Broadway, Cambridge, Massachusetts 02139

Simultaneous Range and Velocity Measurement with Doppler Single-Photon Lidar

RUANGRAWEE KITICHOTKUL,[1,2] JOSHUA RAPP,[2,*] YANTING MA,[2] AND HASSAN MANSOUR[2]

[1] *Department of Electrical and Computer Engineering, Boston University, Boston, Massachusetts 02215, USA*
[2] *Mitsubishi Electric Research Laboratories, Cambridge, Massachusetts 02139, USA*
[*] *rapp@merl.com*

Abstract: Single-photon lidar (SPL) can accurately measure distances to targets from extremely weak reflections. However, the conventional wisdom holds that pulsed lidar cannot directly measure velocity, unlike other forms of lidar. We present for the first time a detection model for SPL that explicitly includes a target's radial velocity, manifesting as a Doppler shift in the repetition frequency of the received laser pulse train. We propose an approach called Doppler SPL, comprising a pair of methods for jointly estimating range and velocity. Our first method estimates the Doppler shift via Fourier analysis of the detection times. The second method is a maximum likelihood (ML) estimator that can improve the Fourier estimate, and which also enables joint estimation of the flux from signal and background sources. We derive the Cramér–Rao bound for the estimation problem and show via simulations that the ML estimator is statistically efficient across diverse acquisition settings. We also demonstrate simultaneous estimation of range with sub-centimeter accuracy and velocity with 0.1 m/s root mean square error for experimental measurements at 50 frames per second, despite a signal-to-background ratio as low as 0.007. Finally, we present an example of a 3D video reconstruction at 120 fps with per-pixel velocity estimates. With the addition of velocimetry, Doppler SPL has the potential to introduce new capabilities in applications such as atmospheric monitoring or autonomous navigation.

1. Introduction

In 2005, five autonomous vehicles completed DARPA's Grand Challenge course, navigating based on point clouds from lidar sensors [1–4]. Since then, the development of better, faster, and cheaper lidar sensors has exploded [5]. One emerging technology is single-photon lidar (SPL), a form of direct time-of-flight lidar that measures distances from the delays between sequences of transmitted laser pulses and their received echoes. Using single-photon detectors and picosecond time tagging enables SPL to tolerate extremely weak reflections [6–9]. As a result, SPL has found success in a wide variety of applications, including atmospheric monitoring [10], airborne and spaceborne terrestrial mapping [11–13], lunar ranging [14], autonomous navigation [15], underwater depth sensing [16], and consumer devices [17].

In addition to capturing 3D structure, using lidar to measure the velocity of moving objects can contribute important information in many applications. In automotive settings, for instance, velocity information can improve detection of moving pedestrians and vehicles [18–21], correct for motion distortion in point cloud registration [22], or assist in vehicle odometry [23]. However, it is generally assumed that pulsed lidar cannot directly measure velocity. Velocity must instead be estimated by regressing over a sequence of distance measurements and extracting a temporal derivative. In SPL, for example, Jonsson et al. [24, 25] proposed splitting a lidar acquisition into a sequence of sub-frames. A distance estimate is formed for each sub-frame, assuming the scene is quasi-static, and the radial velocity is determined from a polynomial fit to the change in distance over time. Subsequent methods follow this basic framework, either fitting curves or applying Bayesian filtering to estimate velocity from sequences of frame- or sub-frame-based

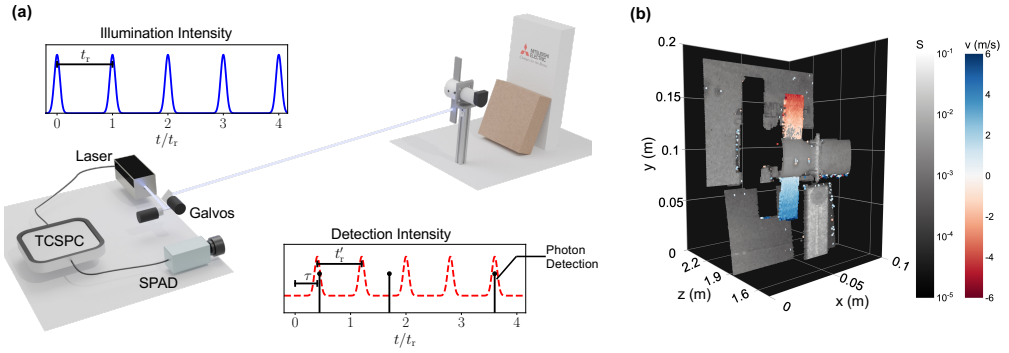

Fig. 1. Overview of Doppler Single-Photon Lidar. (a) A laser transmits short light pulses towards a point in the scene, directed by galvo mirrors. The pulse train reflected from a moving object – such as the rotating fan shown here – is scaled by the reflectivity, time-shifted by the distance, and Doppler-shifted by the radial velocity. The SPAD detects individual photons of reflected light as well as ambient light and time-stamps them with a TCSPC module. (b) Based on the photon detection time sequence we jointly determine the signal flux S (grayscale), 3D position, and velocity v (red-blue color scale, shown for points with $|v| \geq 1\,\mathrm{m/s}$). Further acquisition details for the rotation scene are found in Section 4.2.2 and Visualization 1.

distance measurements [26–30]. One downside is that the component distance measurements, which assume a quasi-static scene, suffer from motion blur at high velocities [31]. Another major challenge in tracking 3D position across multiple measurements is identifying correspondence for objects that also have lateral motion [32, 33], which often requires additional sensors such as conventional cameras [34].

In contrast, several alternative lidar architectures directly measure both range and radial velocity via the Doppler effect, which relates the observed frequency of wave phenomena to the relative velocity between a wave source and observer [35]. Doppler lidar is conventionally based on coherent detection, where the Doppler effect is observed as a shift in the *optical frequency* of the light reflected from a moving target. For instance, frequency-modulated continuous-wave lidar (FMCW) lidar applies triangular frequency modulation to a continuous-wave laser; range and Doppler velocity are then estimated from the sum and difference of a pair of constant beat frequencies. Joint range and velocity sensing – sometimes branded as "4D lidar" – is often touted as an advantage of coherent lidar [36–38]. However, FMCW has other disadvantages compared to time-of-flight systems, particularly that the optical systems are much more complex [39], and the temporal coherence of the laser limits the maximum range [40]. Incoherent systems can also be configured to measure velocity. Heide et al. [41] observed that for amplitude-modulated continuous-wave (AMCW) lidar, a Doppler shift occurs in the *amplitude modulation frequency*, which can be measured with an incoherent detector. However, AMCW is typically limited to indoor environments due to moderate range and resolution capabilties [40], and noise sensitivity can make it difficult to discern low-speed motion [42].

In this paper, we propose an approach to direct velocity measurement called Doppler Single-Photon Lidar (see Fig. 1). Traditionally, SPL has been treated as a form of pulsed lidar, where photon detection times are collected into a temporal histogram and used to estimate only distances [43–45]. Key to Doppler SPL is the recognition that the periodic pulsing of SPL makes it a form of AMCW lidar, so we can observe a Doppler shift between the transmitted *pulse repetition frequency* and the received photon detection sequence. To capture the change in the received pulse frequency, our detection scheme retains not only the photon times relative to the

most recent laser pulse but also the absolute detection times measured with respect to the start of an SPL acquisition. We introduce two methods to estimate velocity from the absolute detection times. Our first method directly estimates the Doppler shift independently of the distance, building on recent advances in Fourier analysis of photon detection times [46]. Our second approach is a maximum likelihood (ML) estimation procedure that jointly optimizes over the velocity and starting distance, as well as the flux levels of signal and background photons. The Fourier approach is not robust to uninformative detections from ambient light and dark counts [47], but it provides a useful initialization for the ML estimator. We show that the ML estimator is robust to strong background light and is statistically efficient, achieving the Cramér–Rao Bound. We validate Doppler SPL through extensive simulations and experiments, successfully demonstrating velocimetry for targets from 0 to 15 m/s and with signal-to-background ratio (SBR) as low as 0.007 photons per period. We also present a 3D video reconstruction of a repetitive scene at 120 frames per second (fps) with per-pixel velocity estimates. The ability to directly measure velocity in addition to distance could impact existing SPL applications (e.g., atmospheric monitoring, autonomous navigation) as well as related photon counting methods in non-line-of-sight imaging [48], quantum sensing [49], and microscopy [50, 51].

2. Measurement Model

Doppler SPL harnesses standard SPL hardware, including a picosecond-pulsed laser and a single-photon avalanche diode (SPAD) detector. The laser emits a periodic sequence of n_r short pulses with repetition period t_r for a total acquisition time $t_\mathrm{a} := n_\mathrm{r} t_\mathrm{r}$. The SPAD detects individual "signal" photons reflected back from the target, as well as "background" photons due to ambient light and dark counts. A time-correlated single-photon counting (TCSPC) module time-stamps the laser pulse times and SPAD detections with picosecond resolution. A pair of galvo mirrors raster scans the laser to form images with the single-pixel detector.

The conventional photon detection model for single-photon lidar assumes a static target [6, 7]. Each pulse travels at the speed of light c, reflects from the target at distance z_0, and returns to the lidar system with a time of flight $\tau_0 = 2z_0/c$. Assuming non-idealities such as dead times and afterpulsing are negligible, photon detection follows an inhomogeneous Poisson process [52] with intensity function

$$\mu(t) = S \left[\sum_{n=0}^{n_\mathrm{r}-1} h(t - \tau_0 - n t_\mathrm{r}) \right] + b, \quad t \in [0, t_\mathrm{a}). \tag{1}$$

The temporal pulse shape is $h(t)$, which we normalize such that $\int_{-\infty}^{\infty} h(t)\,\mathrm{d}t = 1$. The signal flux S is defined as the mean number of detected signal photons per period, which absorbs scaling effects of the illumination power, target reflectivity, view angle, radial fall-off, and detector efficiency. The background is assumed to be constant over the acquisition time with intensity b, so the background flux is $B = b t_\mathrm{r}$, and the signal-to-background ratio (SBR) is S/B. TCSPC records *absolute detection times* $\mathcal{T} := (T_i)_{i=1}^N$ relative to $t = 0$. For static acquisitions, each pulse period has an identical detection time distribution, so often only the *relative detection times* $\mathcal{X} := (X_i)_{i=1}^N$, $X_i = T_i \bmod t_\mathrm{r}$ relative to the most recent laser pulse time are retained in a histogram without loss of information [53].

Instead, we consider the more general case of a target initially at distance z_0 and moving with a constant velocity v, where a positive v indicates a target moving away from the detector. As noted by Heide et al. [41], moving targets cause a Doppler shift in the frequency of a periodic amplitude modulation. We recognize that pulsed illumination can be considered a form of amplitude modulation, so a moving target will likewise cause a Doppler shift in the observed pulse repetition frequency. As we derive in the Supplement, photon detection still follows an inhomogeneous

Poisson process, but the intensity function changes in accordance with the Doppler shift:

$$\lambda(t) = S\left[\sum_{n=0}^{n_\mathrm{r}-1} h\left(t - \frac{c}{c-v}\tau_0 - n\frac{c+v}{c-v}t_\mathrm{r}\right)\right] + b, \quad t \in [0, t_\mathrm{a}). \tag{2}$$

We define the *received* repetition period $t_\mathrm{r}' := ((c+v)/(c-v))t_\mathrm{r}$ and time-of-flight $\tau := (c/(c-v))\tau_0$, as depicted in Fig. 1. Unlike in the static case, the detection time distribution in each pulse period varies due to the velocity, so we retain the absolute detection times $\mathcal{T}$ for estimating v.

3. Estimation Methods

3.1. Static Estimators

Most existing methods for ranging and reflectivity estimation from SPL measurements assume that even dynamic scenes are static over short acquisition times [16, 54–58]. Previously proposed methods for velocimetry with SPL rely on parametric regression over multiple quasi-static distance estimates [24–30]. For a baseline velocity estimator, we follow Jonsson et al. [24] by dividing the acquisition time into L equal sub-frames. The baseline method estimates the distance for each sub-frame by using the ML estimator for static targets [53]. Let $\mathcal{X}_\ell$ denote the relative detection times in the ℓ^{th} sub-frame. Then, the ML estimator for the distance in the ℓ^{th} sub-frame is

$$\widehat{z}_\ell = \underset{z,S,b}{\arg\max} \sum_{X \in \mathcal{X}_\ell} \log\left[Sh\left(X - \frac{2z}{c}\right) + b\right]. \tag{3}$$

The parameters (S, z, b) are initialized using the censoring estimator [9] and then refined by optimizing the objective in (3) using a limited-memory, bound-constrained version of the Broyden–Fletcher–Goldfarb–Shanno algorithm (L-BFGS-B) [59]. Given distance estimates for all sub-frames $\{\widehat{z}_\ell\}_{\ell=1}^{L}$, the baseline method then estimates the velocity and initial distance via linear regression as

$$\widehat{v}, \widehat{z}_0 = \underset{v,z_0}{\arg\min} \sum_{\ell=1}^{L} \left[(z_0 + vt_\ell) - \widehat{z}_\ell\right]^2, \tag{4}$$

where $t_\ell = t_\mathrm{a}(\ell - 1/2)/L$ is the midpoint of the ℓ^{th} sub-frame. We refer to (4) as the *static* estimators. The number of sub-frames L presents a trade-off between motion blur (higher L is better) and robustness (lower L is better). In simulations and experiments, we use $L = 10$; further results demonstrating this tradeoff with $L = 2$ are found in [47] and the Supplement.

3.2. Frequency-domain Estimators

Instead of assuming the scene is quasi-static over short sub-frames, we build upon the constant velocity model in (2). Our first approach aims to estimate the velocity directly from the Doppler-shifted frequency. The velocity is related to the transmitted frequency $f_\mathrm{r} = 1/t_\mathrm{r}$ and received frequency $f_\mathrm{r}' = 1/t_\mathrm{r}'$ as

$$v = c(f_\mathrm{r} - f_\mathrm{r}')/(f_\mathrm{r} + f_\mathrm{r}'). \tag{5}$$

Since f_r is known, our goal is to estimate f_r' from the photon detection times, which we achieve via frequency-domain analysis without preliminary distance estimates. We subsequently consider range estimation in the frequency domain.

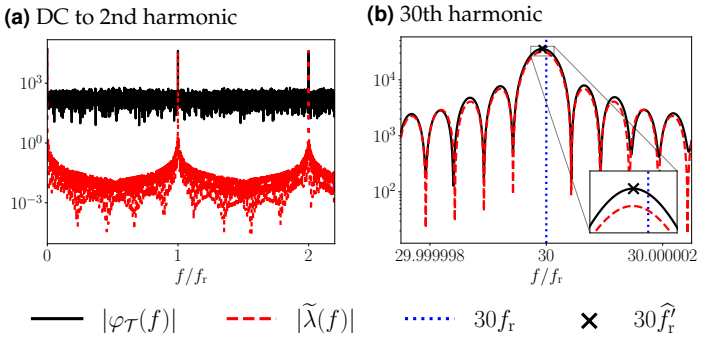

Fig. 2. (a) The magnitudes of the intensity spectrum $\widetilde{\lambda}(f)$ and probed spectrum $\varphi_{\mathcal{T}}(f)$ have peaks around integer harmonics of the received frequency f'_r, which is Doppler-shifted from the transmitted frequency f_r. (b) The Doppler shift is easier to observe at higher harmonics such as $k = 30$.

3.2.1. Flux Probing

We first define the *intensity spectrum* as the Fourier transform of the detection intensity in (2):

$$\begin{aligned}\widetilde{\lambda}(f) = S f'_r t_a \sum_{k=-\infty}^{\infty} \left\{ e^{-j2\pi\left[k f'_r \tau + \frac{t_a}{2}(f - k f'_r)\right]} \widetilde{h}(k f'_r) \operatorname{sinc}[t_a(f - k f'_r)] \right\} \\ + b t_a e^{-j\pi f t_a} \operatorname{sinc}(t_a f),\end{aligned} \tag{6}$$

where $\widetilde{h}(f)$ is the Fourier transform of the pulse shape $h(t)$. Because the modulation in SPL is a pulse train, not a sinusoid, the Doppler shift occurs not only for the fundamental repetition frequency but also for higher harmonics. The spectrum magnitude $|\widetilde{\lambda}(f)|$ thus contains peaks (local maxima) at f'_r and its integer harmonics $\{k f'_r\}_{k\in\mathbb{Z}}$. Background, assumed to be constant, appears as a peak at DC, which negligibly affects the peak positions at higher frequencies. The detection intensity in (2) is implicitly multiplied by an indicator function $\mathbf{1}_{[0,t_a)}$, which transforms to the factors $\{\operatorname{sinc}[t_a(f - k f'_r)]\}_{k\in\mathbb{Z}}$ in the Fourier domain. The longer the acquisition time t_a, the narrower the frequency bands at the harmonics of f'_r, and thus the more precise the velocity estimation in the frequency domain.

We next use tools for Fourier analysis of point processes to compute an approximate spectrum from the detection times. Following Bartlett [60], and more recently Wei et al. [46], the *probed spectrum* given the detection times $\mathcal{T}$ is

$$\varphi_{\mathcal{T}}(f) := \sum_{T\in\mathcal{T}} \exp(-j2\pi f T). \tag{7}$$

Figure 2 shows the probed spectrum $|\varphi_{\mathcal{T}}(f)|$, plotted from a set of experimental detection times, and the intensity spectrum $|\widetilde{\lambda}(f)|$, which uses parameters (S, B, τ_0, v) estimated via the maximum likelihood method we will describe in Section 3C. The transmitted frequency is 40 MHz and the target's velocity is 0.35 m/s, resulting in a −0.094 Hz Doppler shift. We see there are indeed peaks around f'_r and its harmonics, but $|\varphi_{\mathcal{T}}(f)|$ also has a significant noise floor due to the randomness of the photon detection times. Furthermore, randomness in the background detections also contributes to the noise floor and can cause deviations in the peak position around each harmonic. Nevertheless, even small Doppler shifts are visible in the spectrum, especially at higher harmonics, as seen for the 30th harmonic in Fig. 2(b).

3.2.2. Fourier Velocity Estimator

Frequency estimation is often performed by maximizing the periodogram, i.e., the squared magnitude of the spectrum [61]. We follow this basic approach, using the probed spectrum $\varphi_{\mathcal{T}}(f)$ as a proxy for the intensity spectrum $\tilde{\lambda}(f)$. Due to the presence of peaks at harmonics of f_{r}', we are not limited to estimating f_{r}' from a single peak. Instead, we take advantage of the harmonic relationship to propose an estimator based on multiple peaks:

$$\widehat{f_{\mathrm{r}}'} = \underset{f \in [f_{\min}, f_{\max}]}{\arg\max} \sum_{k \in \mathcal{K}} |\varphi_{\mathcal{T}}(kf)|^2 , \tag{8}$$

where $f_{\min}$ and $f_{\max}$ bound the optimization domain for the local maxima, and $\mathcal{K}$ is a set of integers indexing the harmonics of f_{r}'. We solve the nonconcave maximization problem using the L-BFGS-B algorithm initialized to a maximal point from a coarse grid search. The search region $[f_{\min}, f_{\max}]$ is chosen for some reasonable maximum speed $v_{\max}$, where

$$f_{\min} = \frac{c - v_{\max}}{c + v_{\max}} f_{\mathrm{r}}, \quad f_{\max} = \frac{c + v_{\max}}{c - v_{\max}} f_{\mathrm{r}}. \tag{9}$$

Choosing the set of indices $\mathcal{K}$ is a trade-off between accuracy and computation time. Probing only the fundamental frequency f_{r}, i.e., $\mathcal{K} = \{1\}$, is identical to existing methods for frequency estimation that maximize the Bartlett periodogram [62]. When we incorporate higher harmonics, we observe in simulations that using a larger number of harmonics improves the robustness to background detections; details are included in the Supplement. However, the computation time depends linearly on the the number of harmonics $|\mathcal{K}|$. We choose a set of harmonics $\mathcal{K} = \{1, 2, \ldots, k_{\max}\}$ that is as large as possible given the Nyquist rate and computation constraints. According to Wei et al. [46], the Nyquist rate is $f_{\mathrm{Nyquist}} = 1/(2t_{\mathrm{res}})$, where t_{res} is the effective timing resolution of the SPL system, including effects of the quantization of the timing electronics, time jitter, and the laser temporal pulse width. In simulations and experiments, the instrument response function is approximately Gaussian with standard deviation σ, so we use $t_{\mathrm{res}} \approx 4\sigma$. However, a Gaussian pulse assumption is not required, and other measures such as the full width at half maximum (FWHM) could be used to determine the resolution instead. We ensure the maximum probe frequency $k_{\max} f_{\max}$ does not exceed the Nyquist rate. We may also choose $k_{\max}$ to be smaller than the value dictated by the Nyquist rate to reduce computation time.

3.2.3. Fourier Distance Estimator

Distance information is encoded in the phase of the probed spectrum. Assuming $b = 0$ and $h(t)$ is real and even, the phase of the intensity spectrum $\widetilde{\lambda}(f)$ at $f = f_{\mathrm{r}}'$ is

$$\arg\left[\widetilde{\lambda}(f_{\mathrm{r}}')\right] \approx (-2\pi f_{\mathrm{r}}' \tau) \bmod 2\pi. \tag{10}$$

We can thus estimate the time-of-flight by evaluating the phase at the estimated received frequency $\widehat{f_{\mathrm{r}}'}$:

$$\widehat{\tau} = \left\{ -\widehat{t_{\mathrm{r}}'} \arg\left[\varphi_{\mathcal{T}}(\widehat{f_{\mathrm{r}}'})\right] / (2\pi) \right\} \bmod \widehat{t_{\mathrm{r}}'}, \tag{11}$$

where $\widehat{t_{\mathrm{r}}'} := 1/\widehat{f_{\mathrm{r}}'}$. Then, the estimate of the initial time-of-flight is $\widehat{\tau_0} = (c - v)\widehat{\tau}/c$, which corresponds to the initial distance estimate $\widehat{z_0} = c\widehat{\tau_0}/2$. However, nonzero background intensity b changes the probed spectrum phase, degrading distance estimation as will be discussed in Section 4. Fortunately, the Fourier velocity estimator does not depend on the distance and is more robust to background.

3.3. Maximum Likelihood Estimators

The Fourier estimators for v and z_0 are computed via the periodogram. However, the periodogram is only an efficient estimator for certain classes of periodic Poisson process intensities [62]. Maximum likelihood estimation tends to yield better results if the process intensity has a known parametric form [63]. Given detection times $\mathcal{T}$, the intensity function in (2) yields the log-likelihood function [52]

$$\mathcal{L}(S, B, \tau_0, v; \mathcal{T}) = -\int_0^{t_a} \lambda(t)\,\mathrm{d}t + \sum_{T\in\mathcal{T}} \log \lambda(T). \tag{12}$$

Assuming $v \ll c$, we show in the Supplement that the log-likelihood can be reasonably approximated as

$$\mathcal{L}(S, B, \tau_0, v) \approx -n_r(S + B) + \sum_{T\in\mathcal{T}} \log\left[Sh\left(T \bmod t_r - \frac{2vT}{c} - \tau_0\right) + \frac{B}{t_r}\right]. \tag{13}$$

This approximation offers a simple interpretation (the target has moved by vT at time T, resulting in a change in the time-of-flight by $2vT/c$) and simplifies our subsequent Cramér–Rao bound analysis. The ML estimators are

$$\widehat{S}, \widehat{B}, \widehat{\tau}_0, \widehat{v} = \underset{S,B,\tau_0,v}{\arg\max}\, \mathcal{L}(S, B, \tau_0, v). \tag{14}$$

If any of the parameters S, B, τ_0, or v are known or estimated a priori, they can be fixed in the ML estimation. Otherwise, all parameters are jointly estimated.

The optimization problem in (14) is hard, because the objective is non-concave in τ_0 and v. A practical implementation of (14) is to initialize the four parameters with a preliminary estimator and then apply a gradient-based optimization routine to refine the solution. In our simulation and experiments, we initialize v using the Fourier velocity estimator. We then compute motion-compensated relative detection times $\widetilde{X}_i = T_i \bmod t_r - 2\widehat{v}T_i/c$ and apply methods for static targets to obtain initial estimates of the other three parameters from $\widetilde{\mathcal{X}} = (\widetilde{X}_i)_{i=1}^N$. Specifically, we jointly estimate signal and background fluxes using the censoring estimator [9], which has been shown to be a fast approximation of the ML estimator for static targets [53]. Given the signal flux estimate $\widehat{S}$ and the background flux estimate $\widehat{B}$, we apply the ML distance estimator for the initial time-of-flight [7]:

$$\widehat{\tau}_0 = \underset{\tau_0}{\arg\max} \sum_{\widetilde{X}\in\widetilde{\mathcal{X}}} \log\left(\widehat{S}h(\widetilde{X} - \tau_0) + \widehat{B}\Big/t_r\right). \tag{15}$$

Given an initialization $\widehat{S}$, $\widehat{B}$, $\widehat{\tau}_0$, and $\widehat{v}$, we compute (14) using the L-BFGS-B algorithm [59]. While the procedure does not guarantee that its solutions reach global optimal points, we find empirically that they are statistically efficient, as discussed in Section 3D and demonstrated in Section 4A.

3.4. Cramér–Rao Bound

Assuming some regularity conditions, the Cramér–Rao Bound (CRB) states that the inverse of the Fisher information matrix (FIM) is a lower bound for the covariance matrix – and thus the mean-square error – of any unbiased estimator in a statistical estimation problem [64]. In the Supplement, we show that the FIM for all 4 parameters is approximately block-diagonal, implying that efficient estimates of S and B are approximately independent of those for τ_0 and v. We thus focus only on the CRB for τ_0 and v in this section. The 2×2 FIM about τ_0 and v for the

Doppler SPL measurement model is

$$\mathcal{I} = H \begin{bmatrix} n_\mathrm{r} & n_1 \\ n_1 & n_2 \end{bmatrix}, \tag{16}$$

where

$$H := S \int_0^{t_\mathrm{r}'} \left[\frac{h'(t-\tau_0)^2}{h(t-\tau_0) + b/S} - h''(t-\tau_0) \right] \mathrm{d}t\,, \tag{17}$$

$$n_1 := \sum_{n=0}^{n_\mathrm{r}-1} \left(\frac{2(nt_\mathrm{r}' + \tau_0)}{c} \right), \quad n_2 := \sum_{n=0}^{n_\mathrm{r}-1} \left(\frac{2(nt_\mathrm{r}' + \tau_0)}{c} \right)^2, \tag{18}$$

and $h'(t)$ and $h''(t)$ are the first and second temporal derivatives of the pulse shape $h(t)$, respectively. Suppose $\widehat{\theta} = [\widehat{\tau}_0\ \widehat{v}]^T$ is an unbiased estimate of $\theta = [\tau_0\ v]^T$ from some observed detection times $\mathcal{T}$ given that S and B are known. Then,

$$\mathrm{Cov}(\widehat{\theta}) = \mathbb{E}\left[(\widehat{\theta} - \theta)(\widehat{\theta} - \theta)^T \right] \succeq \mathcal{I}^{-1}, \tag{19}$$

i.e., $\mathrm{Cov}(\widehat{\theta}) - \mathcal{I}^{-1}$ must be a positive semidefinite matrix. Consequently, the root-mean-square errors (RMSE) of $\widehat{\tau}_0$ and $\widehat{v}$ are lower bounded by the diagonal entries of the inverse FIM:

$$\mathrm{RMSE}(\widehat{\tau}_0, \tau_0) \geq \sqrt{(\mathcal{I}^{-1})_{11}}, \tag{20}$$

$$\mathrm{RMSE}(\widehat{v}, v) \geq \sqrt{(\mathcal{I}^{-1})_{22}}. \tag{21}$$

We derive the CRB for joint estimation of S, B, τ_0, and v in the Supplement. In simulations and experiments, we refer to the lower bound on the RMSE simply as "CRB."

4. Results

4.1. Simulations

We first present simulations in which ground truth parameters are precisely known. For the results shown in Figures 3 and 4, we fix $S = 0.1$, $\tau_0 = 500\,\mathrm{ns}$, $t_\mathrm{r} = 1\,\mu\mathrm{s}$, and $n_\mathrm{r} = 10^4$. The temporal pulse shape is Gaussian with scaling parameter $\sigma = 0.1\,\mathrm{ns}$. We run 5000 Monte Carlo trials for each setting. In Fig. 3, we investigate the effect of the target velocity on estimation performance varying the velocity from $-50\,\mathrm{m/s}$ to $50\,\mathrm{m/s}$. We examine scenarios with B fixed to 0, 0.01, or 0.1, corresponding to SBRs of ∞, 10, or 1. We observe that the Fourier and ML estimators, which include radial velocity in the acquisition model, maintain the same performance regardless of the velocity. In contrast, the static baseline, which ignores motion within each sub-frame, has greater error as the velocity increases.

However, the performance is not consistent across all SBR levels. The Fourier method significantly degrades as the SBR decreases. In particular, the distance estimator, which assumes negligible background, has RMSE increase by two orders of magnitude from SBR = ∞ to SBR = 10. Meanwhile, the ML estimator continues to remain statistically efficient, achieving the CRB. This effect is explored in greater depth in Fig. 4, where the velocity is fixed to $30\,\mathrm{m/s}$, and B decreases from 10 to 0.01, corresponding to increasing SBR from 0.01 to 10. Indeed, the ML estimator achieves the CRB for all SBR levels. The CRB for both distance and velocity only increases by approximately 8% in this SBR range, demonstrating the ML estimator's robustness to background photons. Additional experiments in the Supplement further demonstrate the advantages of the ML estimator, including a robustness to short acquisition times, small numbers of signal photons, and model mismatch (e.g., non-zero acceleration and varying signal flux). We also show in the Supplement that Doppler SPL estimates outperform quasi-static measurements when used as the input to a Kalman filter.

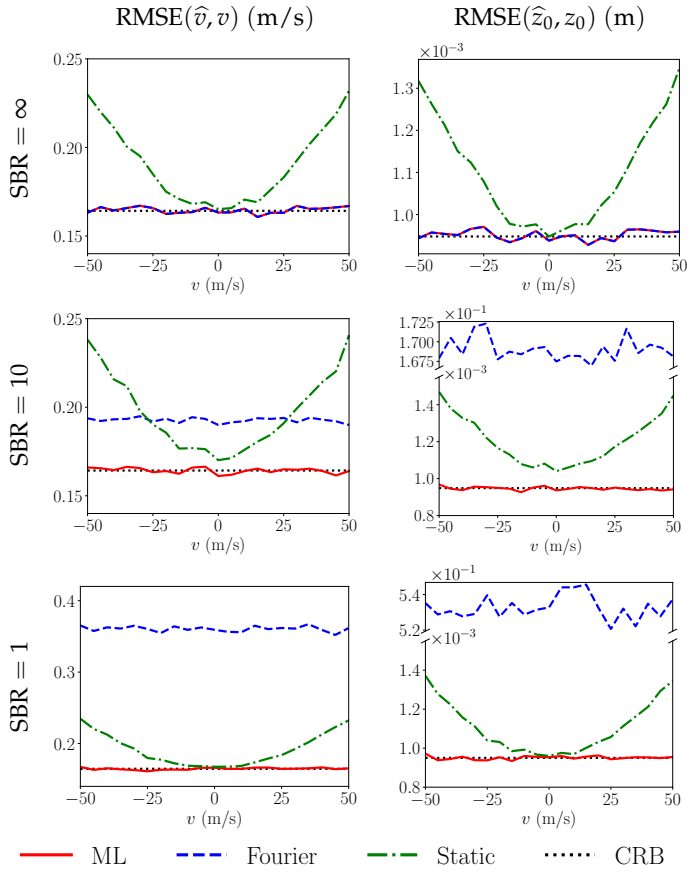

Fig. 3. RMSE and CRB of velocity and range estimates for moving targets with different velocities and SBRs.

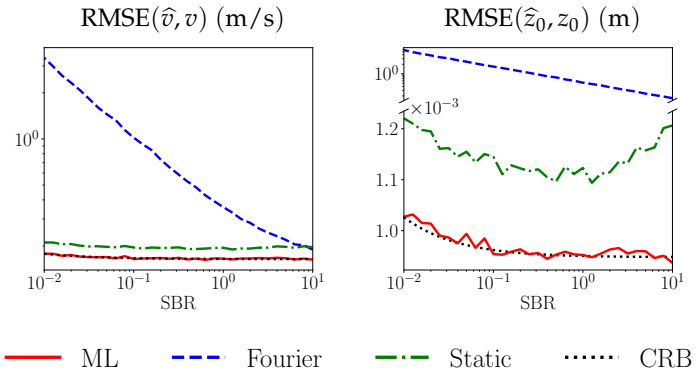

Fig. 4. RMSE and CRB of velocity and range estimates of a target with velocity 30 m/s under different background fluxes.

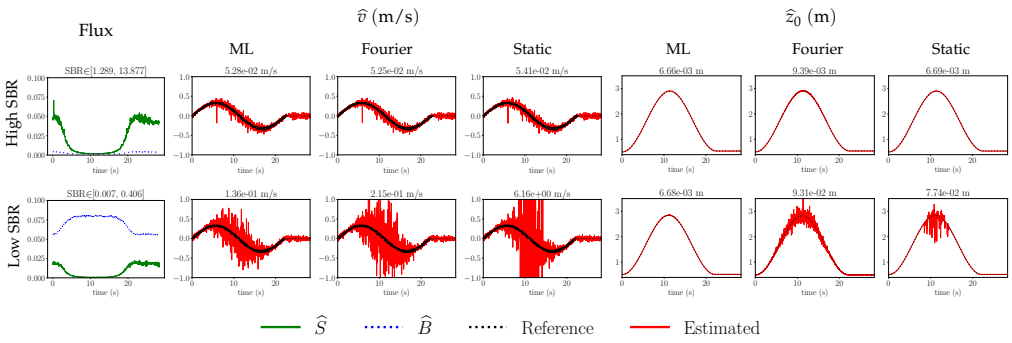

Fig. 5. Experimental demonstration of translational motion estimation using Doppler SPL. The target moves in a line along the optical axis. The leftmost column shows ML estimates of S and B and the corresponding range of values for SBR = $\widehat{S}/\widehat{B}$. The rest of the plots show estimates of initial distances z_0 and velocities v from ML, Fourier, and static estimators, as well as the reference measurements from a linear encoder. The RMSEs of the estimates with respect to the reference are displayed above each plot. See Visualization 1 for a video of the acquisition.

4.2. Experiments

We next validate our approach through a series of experiments. The SPL system uses a pulsed laser at 450 nm (PicoQuant Prima) and a silicon SPAD detector (ID Quantique ID100-50-ULN). Laser synchronization pulses and SPAD events are time stamped via a TCSPC module (Swabian Instruments Time Tagger Ultra). The combined instrument response function is approximately Gaussian with $\sigma = 97$ ps, corresponding to a FWHM width of 228.4 ps. We observe that the transmitted pulse period differs from the nominal value of $t_r = 25$ ns (i.e., $f_r = 40$ MHz) for the laser. Although deviations on the order of femtoseconds are negligible for static measurements, proper calibration is important for estimating small Doppler shifts. Additional experimental details, including our procedure for calibrating t_r and photographs of the setups, are contained in the Supplement.

4.2.1. Translational Motion

We first investigate velocity estimation under linear translational motion. A custom linear motion stage was constructed with T-slot framing and a sliding belt-driven carriage controlled by a hybrid stepper motor. A position reference was measured with a draw-wire linear encoder synchronized to the detection times. The collected detection times are split into contiguous frames of size 0.02 s (i.e., 50 fps) and $n_r \approx 8 \times 10^5$ pulses per frame. Note that this definition of a "frame" differs from the high-speed binary readout from some SPAD arrays that records at most one detection event per frame [65, 66]. We apply the ML, Fourier, and static estimators to the detection times to yield velocity and range estimates. The ML estimator also returns signal and background flux estimates.

Figure 5 highlights two experiments in which the motion stage was programmed to follow a raised cosine trajectory, and parameter estimation was performed for varying laser power and ambient light levels. Within each experiment, the signal flux varies with the target position due to radial fall-off, and the background flux varies with the target position due to changing occlusion of the ambient light. The distance and velocity estimation accuracy also varies with the target position, since the SBR and detection rate are changing. At high SBR, with $\widehat{S}/\widehat{B}$ ranging from 1.289 to 13.877, all methods have similar performance, achieving velocity RMSE around 5 cm/s and sub-centimeter distance accuracy. Motion blur effects are minor for the static estimator

due to the low target velocity. We note that all methods show a negative spike in the velocity estimates at $t = 5.93$ s, which coincides with an anomalous t_r estimate for that frame (see the Supplement for more detail). This underscores the need for careful calibration of t_r to achieve accurate velocity estimates.

At low SBR, with $\widehat{S}/\widehat{B}$ reaching as low as 0.007, the RMSE differences are much larger. The ML estimator has the lowest error for both range and velocity estimation. The ML velocity RMSE increases by a factor of 2.6, whereas the range RMSE is effectively unchanged from the high SBR experiment. In contrast, the Fourier velocity RMSE increases by 4.1×, both the Fourier and static range RMSEs increase by roughly 10×, and the static velocity RMSE increases by over 100×. In accordance with the simulation results, both the Fourier and static estimators are sensitive to low SBR, although they exhibit different types of errors. Further experiments in the Supplement show that increasing the signal flux and the acquisition duration improve estimation accuracy. However, a longer acquisition duration also increases the risk of model mismatch, particularly when the velocity varies or objects enter and exit the field of view during a frame.

4.2.2. Rotational Motion

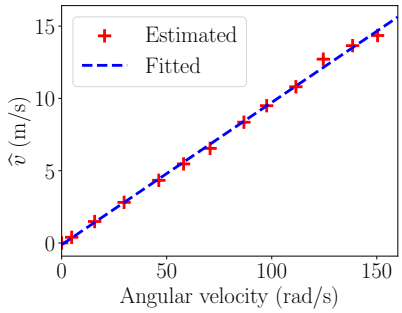

Fig. 6. ML estimates of the radial velocity from captured Doppler SPL measurements of a rotating fan versus angular velocity from the angular encoder. See Visualization 1 for a video of the acquisition.

We next perform experiments with a rotating target, which can achieve much higher radial velocity than the linear motion stage. A rotating fan was custom-built from a DC motor, an aluminum bar, and a 3D-printed mount. An angular encoder connected to the motor provided angular reference measurements that were synchronized to the TCSPC module. In the first rotational motion experiment, we vary the motor speed and take a measurement for a single point on the fan blades. For each fixed motor speed, we extract the frame of length 0.01 s containing the most detections, corresponding to the moment when the fan blades are normal to the laser. We estimate the velocity by applying the ML estimator (14) to the detection times within the frame. In rotational motion, the linear velocity of a point equals the angular velocity times the radius. Hence, we expect a linear trend between the estimated velocity using Doppler SPL and the angular velocity recorded by the motor's encoder. The result shown in Fig. 6 confirms this prediction, demonstrating Doppler SPL's ability to estimate velocity accurately across a wide range of speeds (0 to 15 m/s) using real measurements.

In our final experiment, we capture the entire 3D scene of the rotating fan using Doppler SPL. Ideally, measurements for all pixels of a moving scene would be captured simultaneously using a SPAD array and a flash illumination source. However, since we are limited to a single-element SPAD, we instead use a pair of galvo mirrors to raster scan the laser over the scene with 128×128 pixel resolution. Due to the limited scan rate of our galvos, we capture the full dynamics of the scene for one pixel at a time before moving to the next pixel. The repetitive nature of the

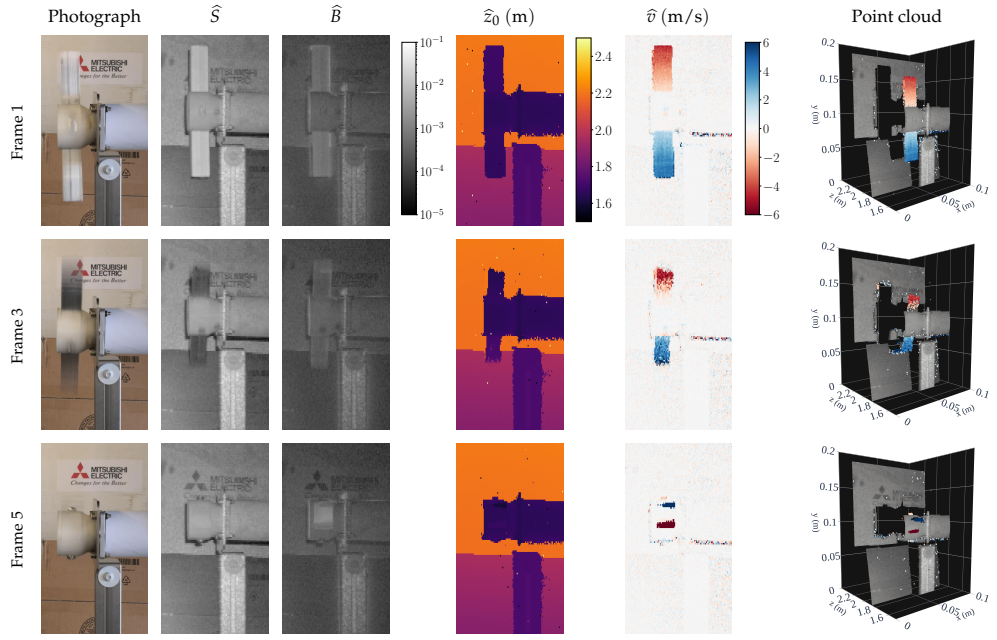

Fig. 7. Demonstration of 3D + velocity imaging using Doppler SPL. The scene consists of a fan with a 10 cm-long blade rotating at 40.3 rad/s (see Photograph). ML estimates of the signal flux S, background flux B, initial distance z_0, and velocity v are determined for detection times grouped into frames of length 8.33 ms (120 fps), synchronized by an angular encoder connected to the fan motor. The rightmost column combines $\widehat{S}$, $\widehat{z}_0$, and $\widehat{v}$ estimates into point clouds. Points with $\widehat{v} \geq 1$ m/s are colored red-blue; all other points show $\widehat{S}$ in grayscale. See Visualization 1 for acquisition and reconstruction videos.

rotational motion allows us to re-synchronize the measurements across different scan positions by matching the motor angles from the encoder readings and emulating array measurements, as in the experiments by Wei et al. [46]. We divide the measurements for each scan location into contiguous frames at 120 fps. We calibrate t_r for each frame and estimate the scene parameters using the ML estimator (14). In Fig. 7 we present the ML estimates of each parameter for selected frames, as well as an approximate photograph aligned to the scene position and a point cloud that combines the signal flux, distance, and velocity maps into a single representation. A video reconstruction for all frames is included in Visualization 1.

The range and velocity estimates agree with the expected rotational motion. The fan rotates such that the top blade moves toward the detector, resulting in negative velocity estimates, and vice versa. The blade length is approximately 10 cm and the angular velocity measured by the encoder is 40.3 rad/s, so the edges of the fan blades move at around 4 m/s when they are perpendicular to the detector, which is confirmed in Frame 1 of Fig. 7. The signal flux estimate $\widehat{S}$ is proportional to the reflectivity, so it reveals fine details in the scene such as the text printed on the cardboard. The background flux estimate $\widehat{B}$ partly reveals the shape of the scene due to multipath reflections from our experimental enclosure. These results demonstrate the potential for Doppler SPL to simultaneously estimate the signal flux, background flux, range, and velocity for fast targets, allowing video reconstruction of textured 3D scenes with per-pixel velocity estimates.

5. Conclusion

We demonstrate in this paper that, counter to the conventional wisdom, SPL can directly measure velocity in addition to range. We derive an ML estimator and show through simulation and experiments that it is robust to a wide range of SBR levels and velocities. Despite the nonconvex ML estimation problem, our Fourier-based estimator of the Doppler shift provides a sufficient initialization to achieve statistically optimal results.

One challenge of SPL is the high data throughput requirements when combining the desire for high spatial and temporal resolution. This is a particular challenge when considering detector arrays, which would be necessary for joint range and velocity estimation of non-repetitive scenes. SPAD arrays with in-pixel time-to-digital converters (TDCs) also have a fixed bit depth that can be allocated towards high time resolution or wide full-scale range, but not both. A recent trend in SPL is the development of alternatives to detection time histograms to reduce the data throughput [67–72]. However, Doppler SPL – as well as compensation for dead times [73–77] and ultra-wideband single-photon imaging [46] – requires the retention of the absolute detection times, recorded at high resolution over many pulse periods. Current alternative data representations are likely incompatible with methods that need to preserve the order of photon detections. Doppler SPL using SPAD arrays will require the development of both compressive representations and the corresponding readout architectures to preserve both distance and velocity information.

The introduction of velocimetry for SPL also opens the door to pursuing many of the same questions that have previously been addressed for distance and reflectivity imaging, such as how to achieve good velocity accuracy at long range [78], with few photons [7], underwater [16], through obscurants [57], in real time [55], etc., as well as the effects of non-idealities such as dead times, afterpulsing, or the drift in the repetition period. Furthermore, the introduction of radial velocity into the acquisition model suggests the need for a more complete model of how motion affects SPL acquisition. For imaging applications, transverse components of the full velocity vector are typically measured via optical flow, which has recently been investigated for indirect ToF [42, 79]. Applications that have lower requirements on spatial resolution, such as wind measurement [80] or space navigation [81, 82], may use three or more laser beam directions to estimate the full velocity vector. Similar approaches could be adapted to work with Doppler SPL. In addition, our frame-wise processing approach does not account for mid-frame occlusion, such as when the fan blade enters a pixel midway during the acquisition, which is mitigated by a high frame rate. A more sophisticated solution could instead perform online reconstruction from the detection times directly [66] or use flexible frame durations and incorporate change detection that accounts for occlusions in dynamic scenes [83, 84]. Finally, a better understanding is needed of the differences in capabilities between SPL, FMCW, and AMCW for capturing distance and velocity information given particular frame rates, power constraints, etc.

Acknowledgment. This work was completed while R. Kitichotkul was an intern at MERL. The authors thank Dr. W. Yerazunis for his invaluable assistance in the design and construction of the experimental testbed and Dr. K. Berntorp for advice on dynamic systems. Portions of this work, including the measurement model and the frequency-domain estimators, were presented at the IEEE International Conference on Acoustics, Speech, and Signal Processing in 2025 [47].

Disclosures. All authors: Mitsubishi Electric Research Laboratories (E,P).

Data availability. Data underlying the results presented in this paper are not publicly available at this time but may be obtained from the authors upon reasonable request.

Supplemental document. See Supplement 1 and Visualization 1 for supporting content.

References

1. S. Thrun, M. Montemerlo, H. Dahlkamp, *et al.*, "Stanley: The robot that won the DARPA Grand Challenge," J. Field Rob. **23**, 661–692 (2006).

2. C. Urmson, C. Ragusa, D. Ray, *et al.*, "A robust approach to high-speed navigation for unrehearsed desert terrain," J. Field Rob. **23**, 467–508 (2006).
3. P. G. Trepagnier, J. Nagel, P. M. Kinney, *et al.*, "KAT-5: Robust systems for autonomous vehicle navigation in challenging and unknown terrain," J. Field Rob. **23**, 509–526 (2006).
4. D. Braid, A. Broggi, and G. Schmiedel, "The TerraMax autonomous vehicle," J. Field Rob. **23**, 693–708 (2006).
5. J. Hecht, "Lidar for self-driving cars," Opt. & Photonics News **29**, 26–33 (2018).
6. A. Kirmani, D. Venkatraman, D. Shin, *et al.*, "First-photon imaging," Science **343**, 58–61 (2014).
7. D. Shin, A. Kirmani, V. K. Goyal, and J. H. Shapiro, "Photon-efficient computational 3-D and reflectivity imaging with single-photon detectors," IEEE Trans. Comput. Imaging **1**, 112–125 (2015).
8. Y. Altmann, X. Ren, A. McCarthy, *et al.*, "Lidar waveform-based analysis of depth images constructed using sparse single-photon data," IEEE Trans. Image Process. **25**, 1935–1946 (2016).
9. J. Rapp and V. K. Goyal, "A few photons among many: Unmixing signal and noise for photon-efficient active imaging," IEEE Trans. Comput. Imaging **3**, 445–459 (2017).
10. R. A. Barton-Grimley, R. A. Stillwell, and J. P. Thayer, "High resolution photon time-tagging lidar for atmospheric point cloud generation," Opt. Express **26**, 26030–26044 (2018).
11. T. Markus, T. Neumann, A. Martino, *et al.*, "The Ice, Cloud, and land Elevation Satellite-2 (ICESat-2): Science requirements, concept, and implementation," Remote. Sens. Environ. **190**, 260–273 (2017).
12. H. Xie, Q. Xu, D. Ye, *et al.*, "A comparison and review of surface detection methods using MBL, MABEL, and ICESat-2 photon-counting laser altimetry data," IEEE J. Sel. Top. Appl. Earth Obs. Remote. Sens. **14**, 7604–7623 (2021).
13. Y. Hong, S. Liu, Z.-P. Li, *et al.*, "Airborne single-photon LiDAR towards a small-sized and low-power payload," Optica **11**, 612–618 (2024).
14. J. O. Dickey, P. L. Bender, J. E. Faller, *et al.*, "Lunar laser ranging: A continuing legacy of the Apollo program," Science **265**, 482–490 (1994).
15. J. Rapp, J. Tachella, Y. Altmann, *et al.*, "Advances in single-photon lidar for autonomous vehicles: Working principles, challenges, and recent advances," IEEE Signal Process. Mag. **37**, 62–71 (2020).
16. A. Maccarone, F. M. D. Rocca, A. McCarthy, *et al.*, "Three-dimensional imaging of stationary and moving targets in turbid underwater environments using a single-photon detector array," Opt. Express **27**, 28437–28456 (2019).
17. S. Rangwala, "The iPhone 12 - LiDAR at your fingertips," Forbes (2020). https://www.forbes.com/sites/sabbirrangwala/2020/11/12/the-iphone-12lidar-at-your-fingertips/.
18. Z. Lin, M. Hashimoto, K. Takigawa, and K. Takahashi, "Vehicle and pedestrian recognition using multilayer lidar based on support vector machine," in *Int. Conf. Mechatron. Mach. Vis. Pract. (M2VIP),* (2018).
19. X. Peng and J. Shan, "Detection and tracking of pedestrians using Doppler lidar," Remote. Sens. **13** (2021). Art. no. 2952.
20. Y. Jin, Y. Kuang, M. Hoffmann, *et al.*, "Radar and lidar deep fusion: Providing Doppler contexts to time-of-flight lidar," IEEE Sensors J. **23**, 25587–25600 (2023).
21. L. Alexandrino, H. Z. Olyaei, A. Albuquerque, *et al.*, "3D object detection for self-driving vehicles enhanced by object velocity," IEEE Access **12**, 8220–8229 (2024).
22. B. Hexsel, H. Vhavle, and Y. Chen, "DICP: Doppler iterative closest point algorithm," in *Proceedings of Robotics: Science and Systems,* (New York City, NY, USA, 2022).
23. Y. Wu, D. J. Yoon, K. Burnett, *et al.*, "Picking up speed: Continuous-time lidar-only odometry using Doppler velocity measurements," IEEE Rob. Autom. Lett. **8**, 264–271 (2023).
24. P. Jonsson, J. Hedborg, M. Henriksson, and L. Sjöqvist, "Reconstruction of time-correlated single-photon counting range profiles of moving objects," in *Proc. SPIE Electro-Opt. Remote Sens. Photon. Tech. Appl. IX,* vol. 9649 (2015), pp. 11–18.
25. Hedborg, Julia, Jonsson, Per, Henriksson, Markus, and Sjöqvist, Lars, "Time-correlated single-photon counting range profiling of moving objects," in *Int. Laser Radar Conf.*, vol. 119 (EPJ Web of Conferences, 2016). Art. no. 06010.
26. W. Xue, L. Liu, X. Dai, and Y. Luo, "Moving target ranging method for a photon-counting system," Opt. Express **26**, 34161–34178 (2018).
27. C. Wu, W. Xing, Z. Feng, and L. Xia, "Moving target tracking in marine aerosol environment with single photon lidar system," Opt. Lasers Eng. **127**, 105967 (2020).
28. X. Liu, J. Qiang, G. Huang, *et al.*, "Velocity-based sparse photon clustering for space debris ranging by single-photon lidar," arXiv:2401.04147 [physics.data-an] (2024).
29. L. Lyu, D. Li, P. Ma, *et al.*, "Photon-statistics-based IMM Kalman filtering method for moving targets detection using single-photon LiDAR," in *Proc. IEEE Int. Instrum. Meas. Technol. Conf.*, (2024).
30. A. Hou, Y. Hu, Y. Xie, *et al.*, "Full waveform recovery method of moving target for photon counting lidar," IEEE Trans. Geosci. Remote. Sens. **62**, 1–14 (2024). Art no. 5701114.
31. Y. Zhao, W. Hao, S. Chen, *et al.*, "Ranging analysis of a moving target based on the dynamic instrument response function," Opt. Lett. **48**, 5487–5490 (2023).
32. F. Yu, J. Xiao, and T. Funkhouser, "Semantic alignment of LiDAR data at city scale," in *Proc. IEEE/CVF Conf. Comput. Vis. Pattern Recog.*, (Boston, MA, USA, 2015), pp. 1722–1731.
33. W. Yang, Z. Gong, B. Huang, and X. Hong, "Lidar with velocity: correcting moving objects point cloud distortion from oscillating scanning lidars by fusion with camera," IEEE Rob. Autom. Lett. **7**, 8241–8248 (2022).

34. A. Ruget, L. Wilson, J. Leach, *et al.*, "A Plug-and-Play algorithm for 3D video super-resolution of single-photon LiDAR data," arXiv:2412.09427 [eess] (2024).
35. C. Doppler, "Über das farbige Licht der Doppelsterne und einiger anderer Gestirne des Himmels," Abhandlungen der k. Böhm **2**, 465–482 (1842).
36. J. Riemensberger, A. Lukashchuk, M. Karpov, *et al.*, "Massively parallel coherent laser ranging using a soliton microcomb," Nature **581**, 164–170 (2020).
37. H. Jang, J. W. Kim, G. H. Kim, *et al.*, "Simultaneous distance and vibration mapping of FMCW-LiDAR with akinetic external cavity diode laser," Opt. Lasers Eng. **160** (2023). Art. no. 107283.
38. P. Mirdehghan, B. Buscaino, M. Wu, *et al.*, "Coherent optical modems for full-wavefield lidar," in *SIGGRAPH Asia Conf. Papers,* (ACM, Tokyo, Japan, 2024), pp. 1–10.
39. R. Roriz, J. Cabral, and T. Gomes, "Automotive LiDAR Technology: A Survey," IEEE Trans. Intell. Transp. Syst. **23**, 6282–6297 (2022).
40. B. Behroozpour, P. A. Sandborn, M. C. Wu, and B. E. Boser, "Lidar system architectures and circuits," IEEE Comm. Mag. **55**, 135–142 (2017).
41. F. Heide, W. Heidrich, M. Hullin, and G. Wetzstein, "Doppler time-of-flight imaging," ACM Trans. Graph. **34**, 1–11 (2015). Art. no. 36.
42. J. Lee, R. J. Suess, and M. Gupta, "Light-in-flight for a world-in-motion," in *Proc. Eur. Conf. Comput. Vis.*, (Milan, Italy, 2024).
43. J. S. Massa, A. M. Wallace, G. S. Buller, *et al.*, "Laser depth measurement based on time-correlated single-photon counting," Opt. Lett. **22**, 543–545 (1997).
44. M. A. Albota, R. M. Heinrichs, D. G. Kocher, *et al.*, "Three-dimensional imaging laser radar with a photon-counting avalanche photodiode array and microchip laser," Appl. Opt. **41**, 7671–7678 (2002).
45. G. Buller and A. Wallace, "Ranging and three-dimensional imaging using time-correlated single-photon counting and point-by-point acquisition," IEEE J. Sel. Top. Quantum Electron. **13**, 1006–1015 (2007).
46. M. Wei, S. Nousias, R. Gulve, *et al.*, "Passive ultra-wideband single-photon imaging," in *Proc. IEEE/CVF Int. Conf. Comput. Vis.*, (Paris, France, 2023), pp. 8101–8112.
47. R. Kitichotkul, J. Rapp, Y. Ma, and H. Mansour, "Doppler single-photon lidar," in *Proc. IEEE Int. Conf. Acoust., Speech, and Signal Process.*, (Hyderabad, India, 2025), pp. 1–5.
48. D. Faccio, A. Velten, and G. Wetzstein, "Non-line-of-sight imaging," Nat. Rev. Phys. **2**, 318–327 (2020).
49. H. Defienne, W. P. Bowen, M. Chekhova, *et al.*, "Advances in quantum imaging," Nat. Photonics **18**, 1024–1036 (2024).
50. B. Torrado, B. Pannunzio, L. Malacrida, and M. A. Digman, "Fluorescence lifetime imaging microscopy," Nat. Rev. Methods Primers **4**, 1–23 (2024). Art. no. 80.
51. W. Liu, R. Qian, S. Xu, *et al.*, "Fast and sensitive diffuse correlation spectroscopy with highly parallelized single photon detection," APL Photonics **6** (2021). Art. no. 026106.
52. D. L. Snyder and M. I. Miller, *Random Point Processes in Time and Space* (Springer Science & Business Media, 2012).
53. R. Kitichotkul, J. Rapp, and V. K. Goyal, "The role of detection times in reflectivity estimation with single-photon lidar," IEEE J. Sel. Top. Quantum Electron. **30** (2024). Art. no. 8800114.
54. D. B. Lindell, M. O'Toole, and G. Wetzstein, "Single-photon 3D imaging with deep sensor fusion," ACM Trans. Graph. **37** (2018). Art. no. 113.
55. J. Tachella, Y. Altmann, N. Mellado, *et al.*, "Real-time 3D reconstruction from single-photon lidar data using plug-and-play point cloud denoisers," Nat. communications **10** (2019). Art. no. 4984.
56. I. Gyongy, S. W. Hutchings, A. Halimi, *et al.*, "High-speed 3D sensing via hybrid-mode imaging and guided upsampling," Optica **7**, 1253–1260 (2020).
57. R. Tobin, A. Halimi, A. McCarthy, *et al.*, "Robust real-time 3D imaging of moving scenes through atmospheric obscurant using single-photon LiDAR," Sci. Rep. **11** (2021). Art. no. 11236.
58. S. Plosz, A. Maccarone, S. McLaughlin, *et al.*, "Real-time reconstruction of 3D videos from single-photon LiDaR data in the presence of obscurants," IEEE Trans. Comput. Imaging **9**, 106–119 (2023).
59. C. Zhu, R. H. Byrd, P. Lu, and J. Nocedal, "Algorithm 778: L-BFGS-B: Fortran subroutines for large-scale bound-constrained optimization," ACM Trans. Math. Softw. **23**, 550–560 (1997).
60. M. S. Bartlett, "The spectral analysis of point processes," J. R. Stat. Soc. B **25**, 264–281 (1963).
61. D. Rife and R. Boorstyn, "Single tone parameter estimation from discrete-time observations," IEEE Trans. Inform. Theory **20**, 591–598 (1974).
62. D. Vere-Jones, "On the estimation of frequency in point-process data," J. Appl. Probab. **19**, 383–394 (1982).
63. M. Bebbington and R. Zitikis, "A robust heuristic estimator for the period of a Poisson intensity function," Methodol. Comput. Appl. Probab. **6**, 441–462 (2004).
64. S. M. Kay, *Fundamentals of Statistical Signal Processing: Estimation Theory* (Prentice-Hall, Inc., Upper Saddle River, NJ, USA, 1993).
65. R. K. Henderson, N. Johnston, F. Mattioli Della Rocca, *et al.*, "A 192 x 128 time correlated SPAD image sensor in 40-nm CMOS technology," IEEE J. Solid-State Circuts **54**, 1907–1916 (2019).
66. Y. Altmann, S. McLaughlin, and M. E. Davies, "Fast online 3D reconstruction of dynamic scenes from individual single-photon detection events," IEEE Trans. on Image Process. **29**, 2666–2675 (2020).

67. C. Zhang, S. Lindner, I. M. Antolovic, *et al.*, "A 30-frames/s, 252 × 144 SPAD Flash LiDAR with 1728 Dual-Clock 48.8-ps TDCs, and Pixel-Wise Integrated Histogramming," IEEE J. Solid-State Circuts **54**, 1137–1151 (2019).
68. M. P. Sheehan, J. Tachella, and M. E. Davies, "A sketching framework for reduced data transfer in photon counting lidar," IEEE Trans. Comput. Imaging **7**, 989–1004 (2021).
69. V. Poisson, V. T. Nguyen, W. Guicquero, and G. Sicard, "Luminance-depth reconstruction from compressed time-of-flight histograms," IEEE Trans. Comput. Imaging **8**, 148–161 (2022).
70. F. Gutierrez-Barragan, F. Mu, A. Ardelean, *et al.*, "Learned compressive representations for single-photon 3D imaging," in *Proc. IEEE/CVF Int. Conf. Comput. Vis.*, (2023), pp. 10756–10766.
71. A. Ingle and D. Maier, "Count-free single-photon 3D imaging with race logic," IEEE Trans. Pattern Anal. Mach. Int. pp. 1–12 (early access, 2023). Doi: 10.1109/TPAMI.2023.3302822.
72. M. P. Sheehan, J. Tachella, and M. E. Davies, "Spline sketches: An efficient approach for photon counting lidar," IEEE Trans. Comput. Imaging **10**, 863–875 (2024).
73. J. Rapp, Y. Ma, R. Dawson, and V. K. Goyal, "Dead time compensation for high-flux ranging," IEEE Trans. Signal Process. **67**, 3471–3486 (2019).
74. A. Ingle, A. Velten, and M. Gupta, "High flux passive imaging with single-photon sensors," in *Proc. IEEE/CVF Int. Conf. Comput. Vis.*, vol. 2019-June (2019), pp. 6753–6762.
75. J. Rapp, Y. Ma, R. Dawson, and V. K. Goyal, "High-flux single-photon lidar," Optica **8**, 30–39 (2021).
76. A. Ingle, T. Seets, M. Buttafava, *et al.*, "Passive inter-photon imaging," in *Proc. IEEE/CVF Conf. Comput. Vis. Pattern Recog.*, (2021), pp. 8585–8595.
77. Y. Liu, F. Gutierrez-Barragan, A. Ingle, *et al.*, "Single-photon camera guided extreme dynamic range imaging," in *Proc. IEEE/CVF Wint. Conf. Appl. Comput. Vis.*, (2022), pp. 1575–1585.
78. Z.-P. Li, J. Ye, X. Huang, *et al.*, "Single-photon imaging over 200 km," Optica **8**, 344–349 (2021).
79. J. J. Wise and L. Streeter, "Towards optical flow in time-of-flight range imaging using the continuous wavelet transform," IEEE Sens. Lett. **8**, 1–4 (2024).
80. I. Smalikho, "Techniques of wind vector estimation from data measured with a scanning coherent Doppler lidar," J. Atmos. Ocean. Technol. **20**, 276–291 (2003).
81. D. F. Pierrottet, F. Amzajerdian, L. Petway, *et al.*, "Linear FMCW laser radar for precision range and vector velocity measurements," MRS Online Proc. Libr. **1076**, 10760406 (2008).
82. D. Pierrottet, F. Amzajerdian, L. Petway, *et al.*, "Navigation Doppler lidar sensor for precision altitude and vector velocity measurements: flight test results," in *Proc. SPIE 8044, Sensors and Systems for Space Applications IV,* K. D. Pham, H. Zmuda, J. L. Cox, and G. J. Meyer, eds. (2011). Art. no. 80440S.
83. T. Seets, A. Ingle, M. Laurenzis, and A. Velten, "Motion adaptive deblurring with single-photon cameras," in *Proc. IEEE/CVF Wint. Conf. Appl. Comput. Vis.*, (2021), pp. 1945–1954.
84. D. Yao, G. Mora-Martín, I. Gyongy, *et al.*, "Bayesian neuromorphic imaging for single-photon LiDAR," Opt. Express **32**, 25147–25164 (2024).